LASER & PHOTONICS REVIEWS
www.lpr-journal.org

Engineering Quantum Nanophotonic Components from Hexagonal Boron Nitride

*Milad Nonahal, Chi Li, Haoran Ren, Lesley Spencer, Mehran Kianinia, Milos Toth, and Igor Aharonovich**

Integrated quantum photonics (IQP) provides a path to practical, scalable quantum computation, communications and information processing. Realization of an IQP platform requires controlled engineering of many nanophotonic components. However, the range of materials for monolithic platforms is limited by the simultaneous need for high-quality quantum light sources, high optical performance, and availability of scalable nanofabrication techniques. Here, the fabrication of IQP components from the recently emerged material hexagonal boron nitride (hBN), including tapered waveguides, microdisks, and 1D and 2D photonic crystal cavities, is demonstrated. Resonators with quality factors greater than 4000 are achieved, and proof-of-principle complex, free-standing IQP circuitry fabricated from single-crystal hBN is engineered. The results show the potential of hBN for scalable integrated quantum technologies.

1. Introduction

Integrated quantum photonics (IQP) offers a promising pathway to large scale quantum information technologies.[1–3] The main constituents of quantum circuitry are quantum emitters that ideally exhibit a spin-photon interface, and photonic elements that include waveguides, cavities and resonators.[4,5] The overarching goal of the IQP approach is based on coupling optically active emitters to nanophotonic constituents and achieve coherent interactions between the quantum elements and photonic cavities.[6–11] Over the last decade, a significant effort has been devoted to key quantum experiments, including Purcell enhancement, single photon switching, and nonlinear effects at the single photon level, using a variety of material systems.[12–22] However, the ultimate solid-state platform for on-chip IQP circuitry is yet to be established.

Hexagonal boron nitride (hBN) has recently emerged as a promising platform for integrated quantum photonics.[23] hBN hosts numerous bright quantum emitters that can be engineered on demand, as well as a range of optically active spin defects with clear optically detected magnetic resonance signatures. Critically, hBN is a wide bandgap van der Waals material that can easily be exfoliated from its bulk form to a range of thicknesses from a monolayer to a few hundred nanometers to support light propagation across a broad spectral range. This unique combination of photophysical properties spurred interest in engineering quantum photonic circuitry from hBN. To date, proof-of-principle demonstrations of isolated photonic resonators and basic optical elements fabricated from hBN have been reported.[24–31] However, a holistic approach to chip-scale nanofabrication is yet to be unveiled, predominantly, due to challenges in fabrication of hBN as it is a robust material that is chemically inert.

Here, we demonstrate the feasibility of fabricating on-chip and freestanding IQP elements from hBN. Specifically, our objective is to develop a universal, wafer scale, nanofabrication protocol in hBN that can be applied to various photonic components simultaneously. The improvements we have achieved in scalability and quality factor are essential for advancing quantum photonics experiments in 2D material. We focus on the monolithic approach, where entire devices are fabricated entirely from hBN. This approach has numerous advantages, including the ability to minimize coupling losses and to position quantum emitters at the highest field of a cavity.[32] We start by addressing the key issue of hBN fabrication. Next, we engineer all the necessary components of a potential quantum circuit, including waveguides, couplers, splitters, and photonic crystal cavities (PCCs). Finally, to illustrate the full potential of this platform, we demonstrate a fully integrated monolithic IQP chip made entirely of suspended hBN.

M. Nonahal, C. Li, L. Spencer, M. Kianinia, M. Toth, I. Aharonovich
School of Mathematical and Physical Sciences, Faculty of Science
University of Technology Sydney
Ultimo2007, New South Wales, Australia
E-mail: aharonovich@uts.edu.au

M. Toth, I. Aharonovich
ARC Centre of Excellence for Transformative Meta-Optical Systems (TMOS)
University of Technology Sydney
Ultimo2007, New South Wales, Australia

H. Ren
School of Physics and Astronomy
Monash University
Clayton3800, Victoria, Australia

The ORCID identification number(s) for the author(s) of this article can be found under https://doi.org/10.1002/lpor.202300019

DOI: 10.1002/lpor.202300019

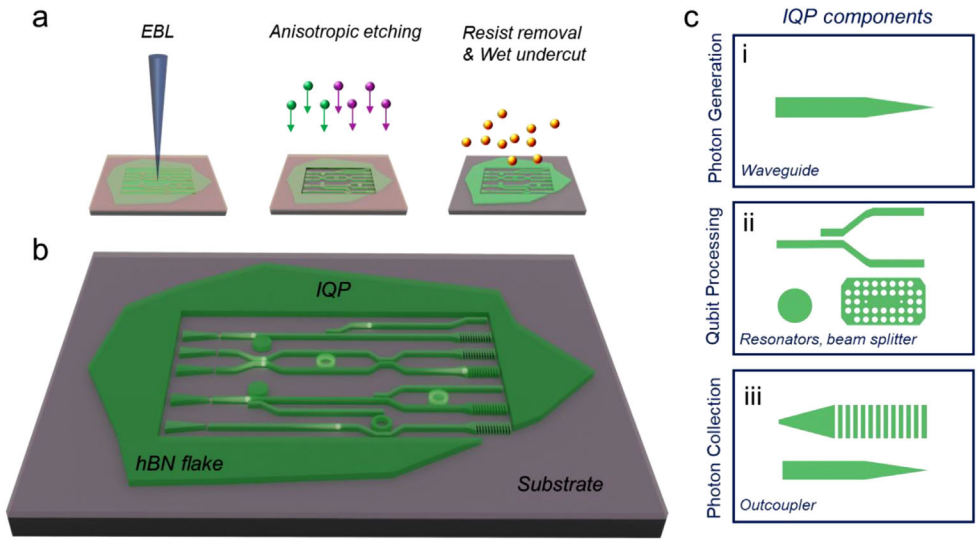

Figure 1. Schematic illustration of monolithic fabrication using hBN. a) Key steps of the fabrication process: electron beam lithography, reactive ion etching, and resist removal. b) Integrated circuit fabricated from single-crystal hBN. c) IQP components: i) low-loss waveguide, ii) resonators, optical cavities, and beam splitter, and iii) out-couplers for detection. Two out-couplers are shown, for top and side collection of photons.

Table 1. Anisotropic dry etch conditions used here and RIE parameters used in prior works on etching of hBN.

Reference	Mask	Chamber pressure	ICP/RIE power	SF6 concentration	Etch rate	Components	Average *Q*-factor
This work	Resist	1 mT	1/300 W	1.5%	5 nm s^{-1}	1D PCC	>2600
						WGMs	≈3200
						2D PCC	≈2000
Froch et al.[28]	Resist	1 mT	50/100 W	10%	–	1D PCC	≈2500
Kuhner et al.[33]	Metal	6 mT	150/300 W	–	4 nm s^{-1}	BIC[a] cavity	≈200
Kim et al.[24]	Resist	10 mT	0/100 W	100%	≈13 nm s^{-1}	2D PCC	160
						1D PCC	≈2000
Ren et al.[27]	Resist	–	40 W	–	–	WGMs	≈1200

[a] Bound state in the continuum (BIC)

The IQP fabrication process is illustrated schematically in **Figure 1**a. Mechanically exfoliated hBN flakes of desired thickness are first identified using an optical microscope and their thicknesses are verified by atomic force microscopy (AFM). A selected flake is then spin-coated with a thin layer of electron-sensitive resist and patterned using electron beam lithography (EBL). After development, the pattern is transferred onto the flake via induced coupled plasma reactive ion etching (ICP/RIE) in a reactive SF_6 gas environment. The sample was immersed in KOH solution to selectively undercut the supporting substrate straight after removing the residual polymer. Figure 1b shows a schematic illustration of a monolithic hBN IQP chip composed of waveguides (photon input), PCCs and resonators (qubit processing), and out-couplers for photon detection. In this work, we demonstrate the ability to fabricate from hBN all basic components of quantum circuitry, as is illustrated explicitly in Figure 1c (i)–(iii). These include waveguides, beam splitters, resonators, optical cavities, and out-couplers used to direct photons to detectors.

2. Results and Discussion

2.1. Device Engineering

Details of the hBN fabrication process are provided in the Experimental Section. Here, we emphasize the key elements needed to achieve high-quality optical components, namely, anisotropic etching and the use of a hard mask that achieves a smooth and vertical sidewall morphology. **Table 1** summarizes the etch parameters used in the current work, and those used in prior works on fabrication of hBN nanophotonic structures. As is demonstrated below, our process yields consistent, smooth etch profiles in a variety of nanostructures. This is achieved primarily by employing a relatively low reactive gas partial pressure and by maximizing ion directionality. To achieve this, a low SF_6 concentration of 1.5 % was employed, the chamber pressure was minimized, and ICP power was also minimized. Under these conditions, ion collisions, ion reflection and reactivity of the plasma are all suppressed, thereby inhibiting lateral etching of hBN. Lateral

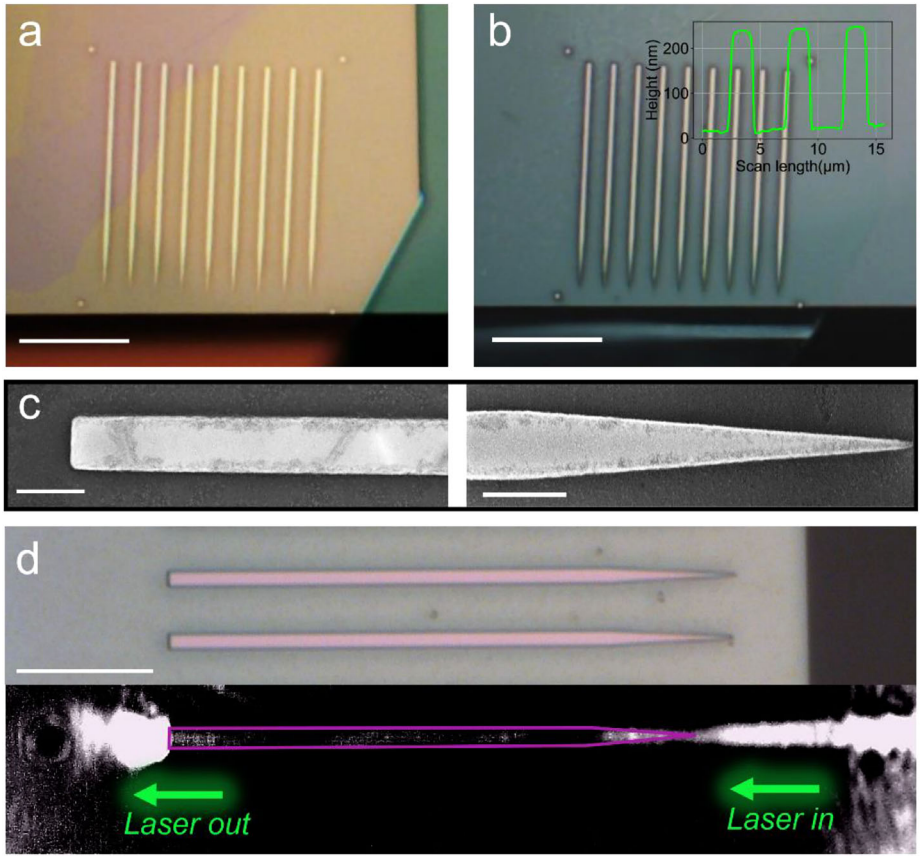

Figure 2. Fabrication and characterization of optical waveguides. Optical images of the a) pre- and b) post-fabricated array of tapered waveguides showing that the structures are fully etched after the RIE step. The scale bar corresponds to 25 μm. Inset: AFM scan profile of the waveguides showing the post-fabricated hBN thickness of ≈200 nm. c) SEM image of two sections of the waveguides. The scale bar is 1 μm. d) magnified optical microscope image of the tapered waveguides illuminated by white light (top) and laser (bottom). The scale bar is 10 μm. The laser power was ≈100 μW in our experiment.

etching produces sloped sidewalls and can give rise to surface roughening, both of which are detrimental to photonic structures and must be minimized.

Our RIE parameters result in very slow etching of the e-beam resist. This makes the resist an excellent hard mask for single-step patterning hBN, thus eliminating the need for a separate liftoff step which can give rise to sidewall roughening. In addition, metal erosion in a highly reactive SF_6 environment can also cause roughening, which is avoided in our process. We note that our etch rate of 5 nm s^{-1} is suitable for chip-scale fabrication, and on par with those of other material systems.

Employing the conditions described above, we fabricated a number of optical components from hBN. First, we engineered waveguides. Optical images of a hBN flake before (after) the etching process are shown in **Figure 2**a,b. Magnified scanning electron microscope images of the taper head and tail sections of the waveguide are shown in Figure 2c. A significant advantage of working with a layered material such as hBN is the ability to transfer the structures between fabrication steps via align transfer method (Experimental Section). To this end, the chosen hBN flake with the correct thickness (≈200 nm) was first identified and patterned in the middle of the substrate, where the fabrication step (resist spin-coating) does not generate edge artifacts. After developing the pattern, the hBN and the resist mask were transferred to the edge of the substrate, so that the tapered waveguides can be effectively used. Finally, the pattern was transferred to the hBN using ICP/IRE. AFM profile of the post-fabricated waveguides confirms the hBN thickness of around 200 nm as shown in Figure 2b inset.

The functionality of the waveguides is demonstrated by optical measurements. The waveguide was excited by a lensed fiber through the tapered area and the light was collected from the tail end of the waveguide as is seen in the bright-field image shown in Figure 2d. Due to the high quality of the fabrication process, minimum scattering is observed in the body of the waveguide, resulting in efficient light confinement, and guiding. The transmission behavior of the waveguides was analyzed via COMSOL Multiphysics simulations showing around 99% transmittance (580 nm incidence) in the propagation distance of 10 μm (Figure S1, Supporting Information) in the monolithic waveguides.

In addition, to showcase the capabilities of the waveguides for IQP purposes, we calculated the coupling efficiency of a quantum emitter within the waveguides. To this end, the integration of a common hBN quantum emitter (possessing zero-phonon line ≈580 nm) was analyzed by placing an in-plane source of quantum emitter into the waveguides (Figure S2, Supporting

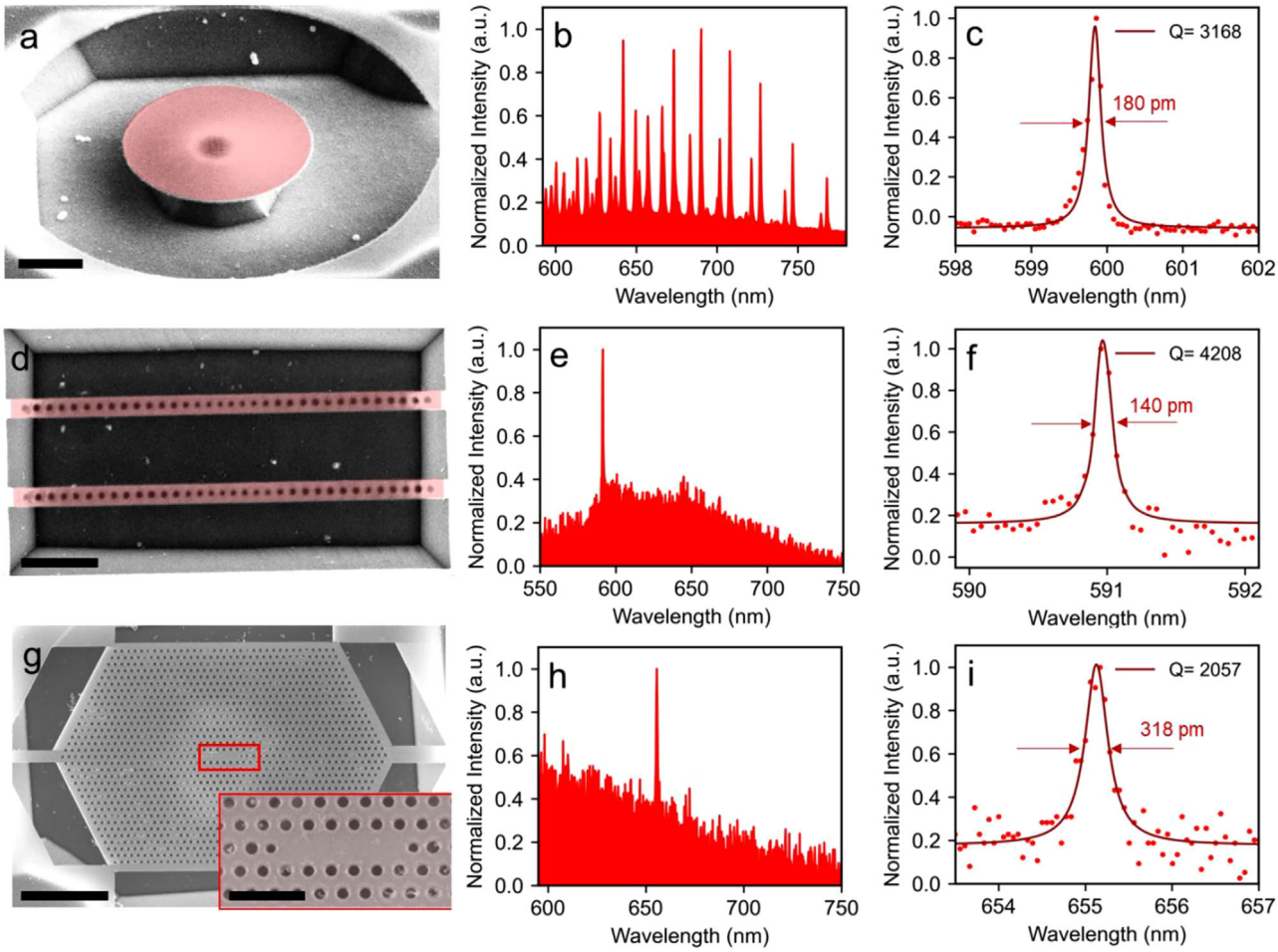

Figure 3. Fabrication and characterization of photonic resonators. a,d,g) False-color SEM images of a suspended hBN microdisk resonator, 1D PCC and 2D PCC, respectively. The scale bars in (a), (d), and (g) correspond to 1, 1, and 4 µm, respectively. g) Inset: Magnified SEM image of the 2D PCC center area. The scale bar corresponds to 1 µm. b,e,h) PL spectra showing WGMs in the microdisk cavity, and resonances in the 1D and 2D PCCs. c,f,i) High-resolution PL spectra showing the widths of the optical cavity modes. The data were fitted with Lorentzian functions to obtain the resonance quality factors ($\lambda/\Delta\lambda$).

Information). The results demonstrate around 30% coupling efficiency for such devices.

2.2. Photonic Resonators

Now we turn to photonic resonators. We focus on three device geometries that are most common in integrated nanophotonics. These are microdisk cavities, and 1D and 2D photonic crystal cavities. Note that suspended cavities are preferred in order to maximize refractive index contrast and hence light confinement within the cavities. The optical loss in such structures was studied using COMSOL simulations and we theoretically observed the field loss of ≈10% and ≈14% for the suspended and supported structures, respectively (Figure S3, Supporting Information).

Suspended architecture is typically achieved by undercutting a sacrificial layer on which the cavity material is grown epitaxially. In our case, we transfer exfoliated hBN flakes onto silicon, and undercut the silicon using a KOH wet chemical etch process. **Figure 3**a shows a tilted, false-color SEM image of a suspended disk resonator (3 µm in diameter) which is supported by a small silicon pillar indicating the feasibility of wet chemical etching to fabricate such small freestanding structures. 10 wt% KOH was used for the Si substrate undercut (refer to the Experimental Section). For the characterization of the cavities, we employed a standard confocal microscope with a variety of excitation sources. The polymer residue on the structures was excited with a 532 nm laser leading to a broad emission which can be used as the light source to study the optical modes. In this case only allowed wavelengths from a broad emission can confine within the cavity as the individual mode. A PL spectrum from the hBN microdisk is shown in Figure 3b. It exhibits a clear set of whispering gallery mode (WGM) resonances, seen as sharp peaks in the spectrum. The multimodal feature of the WGM corresponds to both transverse electric (TE) and transverse magnetic (TM) modes of confined electromagnetic field within the cavity. The superimposed optical modes result from total internal reflection of the relatively high index disk resonator and shows a free spectral range ($=\lambda^2/2n\pi R$) of about 20 nm according to the spectrum.

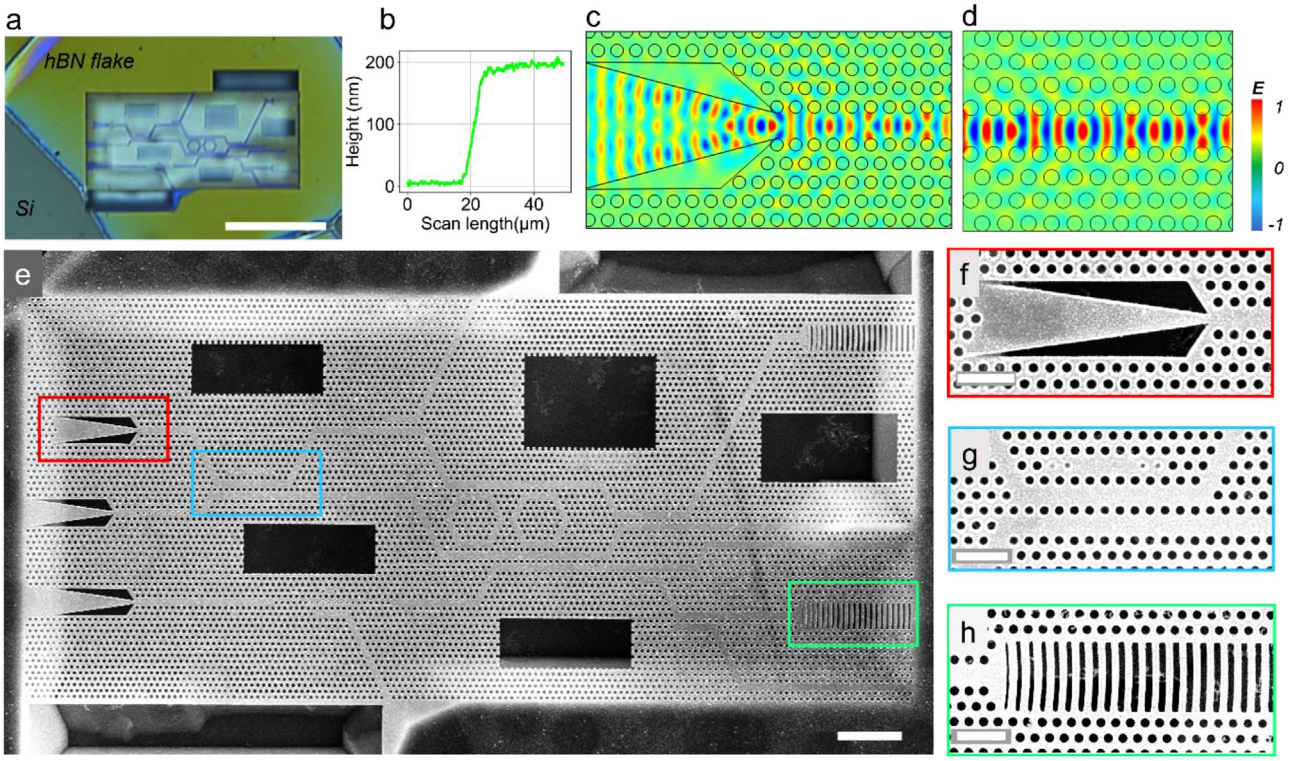

Figure 4. Suspended on-chip IQP circuit fabricated from single-crystal hBN. a) Optical image of the suspended structure embedded in an exfoliated hBN flake. The scale bar corresponds to 20 μm. b) AFM scan profile of the fabricated hBN flake. Simulated electric field distribution of c) tapered and d) straight photonic crystal waveguides. For both simulations, an out-of-plane electric field is incident on the left side of the waveguide structure at a wavelength of 600 nm. e) Top-view SEM image of the circuit. The scale bar corresponds to 3 μm. Three elements are highlighted by red, cyan, and green boxes and zoomed-in images shown in (f)–(h), corresponding to photon generation, manipulation, and detection, respectively. The scale bars in (e)–(g) corresponds to 1 μm.

To obtain the quality factor ($Q = \lambda/\Delta\lambda$), a high-resolution PL spectrum of an individual WGM was recorded and the peak was fitted by a Lorentzian function. The microdisk exhibits a narrow linewidth of 180 pm and a high Q of >3000 (Figure 3c). This represents a sixfold improvement in Q-factor over prior reports.[25] The improvement is predominantly due to the experimental realization of a suspended microdisk resonator from hBN, as well as the improved etch recipe.

Figure 3d is a top-view, false-color SEM image of a 1D hBN PCC. The cavity consists of an array of holes in a waveguide, with a varying diameter (down to 80 nm). The cavity resonance is shown in Figure 3e,f. The resonance width is 140 pm, which corresponds to a Q-factor of >4000 (Figure 3f). Next, we fabricated 2D PCCs. Figure 3g shows an SEM image of a 2D PCC structure (L5 configuration, whereby five holes are linearly eliminated from the central area). A close-up of the cavity center is shown in the inset. The 2D PCC exhibits a single optical mode (Figure 3h) with a modest Q-factor of ≈2000, as is shown in the high-resolution spectrum in Figure 3i. The modest quality factor for the 2D configuration is caused by losses within hBN due to its relatively low refractive index. Nevertheless, for some applications, 2D PCC geometries can be advantageous for scaling up to an on-chip IQP circuitry.

Purcell enhancement, given by $F_p = \frac{3}{4\pi^2}\left(\frac{\lambda}{n}\right)^3 \frac{Q}{V}$, for the above PCCs, can potentially be very high. Given the low mode volume of the 1D PCCs ($V \approx 1.5(\lambda/n)^3$), and the Q-factor of ≈4000, the Purcell enhancement could exceed 200. However, this is hardly achievable due to the difficulty of precisely positioning the emitter within the electric field maxima of the cavity. Note that for monolithic cavities fabricated entirely from hBN, the emitter would be positioned within the high field region of the cavity, rather than coupled evanescently. This should result in substantial overlap with the cavity field, and hence a significant enhancement.[6,34,35]

We conducted a comparative analysis of the average quality factor reported for our hBN cavities with those of other fabrication methods in the literature (as listed in Table 1). Our results show that our method demonstrates a higher degree of versatility in the fabrication of various components. This was also confirmed by a statistical analysis of the Q-factor of several cavities showing an average value of ≈2600 as shown in Figure S4 (Supporting Information). Furthermore, our cavities exhibited consistently higher average quality factors compared to those produced using other methods. This provides strong evidence supporting the effectiveness of our fabrication approach.

Finally, we fabricated a proof-of-concept suspended IQP circuit from a single crystal hBN flake. **Figure 4**a, shows an optical image of the hBN IQP circuit. An exfoliated hBN flake (≈200 nm thick as shown by an AFM scan in Figure 4b) on a silicon substrate is sufficiently large to accommodate the

50 μm × 25 μm circuit, seen as a rectangular region in the optical image. The contrast difference is caused by the selective undercut etch process – the region underneath the circuit was chemically etched by KOH solution, admitted to the silicon substrate through the large rectangular holes seen in Figure 4e. The platform consists of air hole arrays in a hBN slab, specifically a hexagonal lattice with a pitch distance of 300 nm and air holes with a radius of 100 nm. One row of holes was eliminated to perform the waveguide function. For the tapered waveguide, we used triangle couplers with air to taper down the cross section of the guided wave inside the photonic crystal waveguide.

The electromagnetic field guiding in the photonic crystal waveguides were numerically simulated in the COMSOL Multiphysics software. The electric field distributions of the guided waves are given in Figure 4c,d, wherein a linear polarized electric field input (out-of-plane) was placed at the left side of the waveguides. Low-loss wave guiding and propagation in both tapered and straight waveguide structures can be achieved based on our simulation results. Figure 4d shows a top-view SEM image of the IQP circuit. Three main elements are shown on the image, namely data generation (red box), manipulation (cyan) and detection (green). Figure 4f–h shows the higher magnification SEM images of these sections. Although we observed random optical modes in such structure (Figure S5, Supporting Information), we emphasize that the IQP chip was not designed for any specific operation. Rather it shows that all the required components, including couplers, waveguides, PCCs, routers, beam splitters, and out-couplers can be engineered in a single, suspended flake of hBN using a robust nanofabrication method.

These structures can be specifically designed to generate photonic bandgaps for particular wavelengths, and can enable special functionalities such as guiding,[36] making them a promising platform for future applications. In addition, the availability of a wafer-scale and monocrystalline hBN with desired thickness remains a significant challenge in the fabrication of integrated architectures. However, this issue can potentially be resolved through the development of device-scale synthesis methods such as chemical vapor deposition (CVD)[37,38] and high-pressure high-temperature (HPHT)[39] techniques in the future.

Moreover, the integration of quantum emitters into the presented structures can greatly enhance their functionality and pave the way for future quantum photonics applications. However, achieving scalable integration of quantum emitters requires a deterministic and site-specific method of quantum emitter generation. One possible solution for scalable integration is to develop techniques that can generate quantum emitters in a controlled manner and integrate them with the desired structures. These include, for instance, device-scale ion/electron beam irradiation,[40] atomic force microscope indentation,[41] deterministic laser writing,[42] or patterned van der Waals heterostructure assembly.[43]

3. Conclusion

To summarize, we developed a reliable and robust recipe to engineer quantum photonic circuitry from hBN. Specifically, a proof-of-concept fabrication of a chip-scale circuit, with 1D, and 2D photonic resonators have been demonstrated, from a monolithic hBN flake. The suspended architecture yields improved light confinement, with measured Q-factors in excess of 4000 for 1D PCC. Our work marks an important step towards integration of quantum emitters and scalable quantum photonic elements in hBN. It demonstrates a promising pathway to realization of advanced spin–photon interfaces, and deployment of hBN in quantum optomechanics, and in applications based on strong coupling between a quantum emitter and a photonic resonator. Using an on-chip set of low-loss waveguides and optical cavities, IQP can provide coherent quantum circuitry capable of performing core quantum tasks including quantum state generation, manipulation and detection of information.

4. Experimental Section

Fabrication: Monocrystalline hBN flakes were first transferred onto precleaned silicon substrates using tape exfoliation from a larger bulk crystal. The sample was annealed in a programmable tube furnace in an ambient atmosphere. The furnace was programmed to anneal sample at 500 °C for 4 h to remove all tape residue and then at 650 °C for 2 h followed by 850 °C for another 30 min. Such temperature history first assists in increasing the hBN/substrate adhesion substantially as well as oxidizing uncovered silicon surface as compared to the underlying region of the hBN flakes. This specifically helps the undercut underlying patterned region by increasing the etch selectivity of KOH for Silicon compared to superficially oxidized area. Afterward, suitable flakes were identified by optical microscope and further confirmed by AFM. Note that, from exfoliated flakes, only those with thicknesses of 200–300 nm were chosen for the fabrication to provide a sufficient Q-factor. A thin layer of positive e-beam resist (CSAR, AllResist GmbH) was subsequently spin-coated onto the substrate to form ≈300 nm polymer film. The sample was then patterned into the resist using electron beam lithography at 30 keV and 23 pA in a Zeiss Supra coupled with an RAITH EBL. After development, the pattern was transferred into the underlying hBN and silicon substrate using reactive ion etching in a Trion ICP-RIE system at 1 mT, 1.5% SF6, 300 W RIE, 1 W ICP. Finally, the structures were undercut in 10 wt% KOH at room temperature and the resist was then removed using a polymer stripper.

Align Transfer: The fabricated device was precisely transferred onto the edge of a thermal oxide silicon substrate for laser side excitation scheme. This was executed via an align transfer method under an optical microscope equipped with two *x*-*y*-*z* stages with a polymer stamp. The stamp was drop-cast by a thin film of a water-soluble polyvinyl alcohol (PVOH) as a sticking layer to pick the hBN flake. After transfer, the PVOH was dissolved with water and the residual was cleaned in a UV–ozone chamber for 10 min.

Optical Characterization: The Q-factor characterization was performed with the lab-built confocal system. A 532 nm CW laser (Gem 532TM, Laser Quantum Ltd.) was used as the excitation source. The laser was reflected by a 532-nm long pass dichroic mirror into a 100× magnification objective (0.9 NA). Scanning was performed using a scanning mirror. A 550-nm long pass filter was placed after the dichroic mirror and before either the spectrometer (Princeton Instruments, Inc.) for PL spectrum or a single-photon avalanche diode (Excelitas Technologies) for micro-PL mapping. In this work, PL spectra were taken with other low (300 g mm^{-1}) or high (1200 g mm^{-1}) gratings. For searching the cavity modes, the cavities with the photoluminescence from residual polymer were mapped, then checked with the spectrometer while driving and placing the laser spot.

Simulations: The electromagnetic field guiding in the tapered waveguide and photonic crystal waveguide was simulated by a commercial COMSOL Multiphysics software. An out-of-plane linear polarized electric dipole was placed at the left side of the waveguides at the beginning of the simulation. The photonic crystal bandgap of the waveguide was optimized for 600 nm target wavelength, and hBN refractive index of 2.1 (at 600 nm) was used. The corresponding hexagonal pitch is 300 nm, while the hole radius is 100 nm.

Supporting Information

Supporting Information is available from the Wiley Online Library or from the author.

Acknowledgements

This work was supported by the Australian Research Council (CE200100010, DE220101085, and DP220102152) and the Office of Naval Research Global (N62909-22-1-2028).

Open access publishing facilitated by University of Technology Sydney, as part of the Wiley – University of Technology Sydney agreement via the Council of Australian University Librarians.

Conflict of Interest

The authors declare no conflict of interest.

Data Availability Statement

The data that support the findings of this study are available from the corresponding author upon reasonable request.

Keywords

hexagonal boron nitride (hBN), integrated quantum photonics, photonic crystal cavity, waveguides

Received: January 12, 2023
Revised: May 25, 2023
Published online: June 20, 2023

[1] J. Wang, F. Sciarrino, A. Laing, M. G. Thompson, *Nat. Photonics* **2020**, *14*, 273.
[2] Moody, V. J. Sorger, D. J. Blumenthal, P. W. Juodawlkis, W. Loh, C. Sorace-Agaskar, A. E. Jones, K. C. Balram, J. C. Matthews, A. Laing, *J. Phys.: Photonics* **2022**, *4*, 012501.
[3] E. Pelucchi, G. Fagas, I. Aharonovich, D. Englund, E. Figueroa, Q. Gong, H. Hannes, J. Liu, C. Y. Lu, N. Matsuda, *Nat. Rev. Phys.* **2022**, *4*, 194.
[4] J. H. Kim, S. Aghaeimeibodi, J. Carolan, D. Englund, E. Waks, *Optica* **2020**, *7*, 291.
[5] N. H. Wan, T. J. Lu, K. C. Chen, M. P. Walsh, M. E. Trusheim, L. De Santis, E. A. Bersin, I. B. Harris, S. L. Mouradian, I. R. Christen, E. S. Bielejec, D. Englund, *Nature* **2020**, *583*, 226.
[6] A. E. Rugar, S. Aghaeimeibodi, D. Riedel, C. Dory, H. Lu, P. J. McQuade, Z. X. Shen, N. A. Melosh, J. Vučković, *Phys. Rev. X* **2021**, *11*, 031021.
[7] A. Sipahigil, R. E. Evans, D. D. Sukachev, M. J. Burek, J. Borregaard, M. K. Bhaskar, C. T. Nguyen, J. L. Pacheco, H. A. Atikian, C. Meuwly, R. M. Camacho, F. Jelezko, E. Bielejec, H. Park, M. Loncar, M. D. Lukin, *Science* **2016**, *354*, 847.
[8] D. O. Bracher, X. Zhang, E. L. Hu, *Proc. Natl. Acad. Sci. USA* **2017**, *114*, 4060.
[9] D. Rattenbacher, A. Shkarin, J. Renger, T. Utikal, S. Götzinger, V. Sandoghdar, *New J. Phys.* **2019**, *21*, 062002.
[10] E. Schöll, L. Hanschke, L. Schweickert, K. D. Zeuner, M. Reindl, S. F. Covre da Silva, T. Lettner, R. Trotta, J. J. Finley, K. Müller, A. Rastelli, V. Zwiller, K. D. Jöns, *Nano Lett.* **2019**, *19*, 2404.
[11] M. Davanco, J. Liu, L. Sapienza, C. Z. Zhang, J. V. De Miranda Cardoso, V. Verma, R. Mirin, S. W. Nam, L. Liu, K. Srinivasan, *Nat. Commun.* **2017**, *8*, 889.
[12] P. P. J. Schrinner, J. Olthaus, D. E. Reiter, C. Schuck, *Nano Lett.* **2020**, *20*, 8170.
[13] C. Toninelli, I. Gerhardt, A. S. Clark, A. Reserbat-Plantey, S. Gotzinger, Z. Ristanovic, M. Colautti, P. Lombardi, K. D. Major, I. Deperasinska, W. H. Pernice, F. H. L. Koppens, B. Kozankiewicz, A. Gourdon, V. Sandoghdar, M. Orrit, *Nat. Mater.* **2021**, *20*, 1615.
[14] A. Javadi, D. Ding, M. H. Appel, S. Mahmoodian, M. C. Löbl, I. Söllner, R. Schott, C. Papon, T. Pregnolato, S. Stobbe, *Nat. Nanotechnol.* **2018**, *13*, 398.
[15] A. V. Zasedatelev, A. V. Baranikov, D. Sannikov, D. Urbonas, F. Scafirimuto, V. Y. Shishkov, E. S. Andrianov, Y. E. Lozovik, U. Scherf, T. Stöferle, *Nature* **2021**, *597*, 493.
[16] C. P. Dietrich, A. Fiore, M. G. Thompson, M. Kamp, S. Höfling, *Laser Photonics Rev.* **2016**, *10*, 870.
[17] M. Radulaski, J. L. Zhang, Y. K. Tzeng, K. G. Lagoudakis, H. Ishiwata, C. Dory, K. A. Fischer, Y. A. Kelaita, S. Sun, P. C. Maurer, *Laser Photonics Rev.* **2019**, *13*, 1800316.
[18] J. A. Martínez, R. A. Parker, K. C. Chen, C. M. Purser, L. Li, C. P. Michaels, A. M. Stramma, R. Debroux, I. B. Harris, M. H. Appel, *Phys. Rev. Lett.* **2022**, *129*, 173603.
[19] P. J. Stas, Y. Q. Huan, B. Machielse, E. N. Knall, A. Suleymanzade, B. Pingault, M. Sutula, S. W. Ding, C. M. Knaut, D. R. Assumpcao, Y. C. Wei, M. K. Bhaskar, R. Riedinger, D. D. Sukachev, H. Park, M. Lončar, D. S. Levonian, M. D. Lukin, *Science* **2022**, *378*, 557.
[20] S. Boissier, R. C. Schofield, L. Jin, A. Ovvyan, S. Nur, F. H. L. Koppens, C. Toninelli, W. H. P. Pernice, K. D. Major, E. A. Hinds, A. S. Clark, *Nat. Commun.* **2021**, *12*, 706.
[21] O. Iff, Q. Buchinger, M. Moczała-Dusanowska, M. Kamp, S. Betzold, M. Davanco, K. Srinivasan, S. Tongay, C. Antón-Solanas, S. Höfling, C. Schneider, *Nano Lett.* **2021**, *21*, 4715.
[22] L. Li, T. Schröder, E. H. Chen, M. Walsh, I. Bayn, J. Goldstein, O. Gaathon, M. E. Trusheim, M. Lu, J. Mower, M. Cotlet, M. L. Markham, D. J. Twitchen, D. Englund, *Nat. Commun.* **2015**, *6*, 6173.
[23] J. D. Caldwell, I. Aharonovich, G. Cassabois, J. H. Edgar, B. Gil, D. N. Basov, *Nat. Rev. Mater.* **2019**, *4*, 552.
[24] S. Kim, J. E. Froch, J. Christian, M. Straw, J. Bishop, D. Totonjian, K. Watanabe, T. Taniguchi, M. Toth, I. Aharonovich, *Nat. Commun.* **2018**, *9*, 2623.
[25] J. E. Fröch, Y. Hwang, S. Kim, I. Aharonovich, M. Toth, *Adv. Opt. Mater.* **2019**, *7*, 1801344.
[26] C. Li, J. E. Froch, M. Nonahal, T. N. Tran, M. Toth, S. Kim, I. Aharonovich, *ACS Photonics* **2021**, *8*, 2966.
[27] T. Ren, P. Song, J. Chen, K. P. Loh, *ACS Photonics* **2018**, *5*, 353.
[28] J. E. Froch, C. Li, Y. Chen, M. Toth, M. Kianinia, S. Kim, I. Aharonovich, *Small* **2022**, *18*, 2104805.
[29] C. H. Liu, J. Zheng, S. Colburn, T. K. Fryett, Y. Chen, X. Xu, A. Majumdar, *Nano Lett.* **2018**, *18*, 6961.
[30] N. V. Proscia, H. Jayakumar, X. Ge, G. Lopez-Morales, Z. Shotan, W. Zhou, C. A. Meriles, V. M. Menon, *Nanophotonics* **2020**, *9*, 2937.
[31] C. Qian, V. Villafañe, M. Schalk, G. V. Astakhov, U. Kentsch, M. Helm, P. Soubelet, N. P. Wilson, R. Rizzato, S. Mohr, A. W. Holleitner, D. B. Bucher, A. V. Stier, J. J. Finley, *Nano Lett.* **2022**, *22*, 5137.
[32] N. C. Harris, D. Bunandar, M. Pant, G. R. Steinbrecher, J. Mower, M. Prabhu, T. Baehr-Jones, M. Hochberg, D. Englund, *Nanophotonics* **2016**, *5*, 456.
[33] L. Kühner, L. Sortino, B. Tilmann, T. Weber, K. Watanabe, T. Taniguchi, S. A. Maier, A. Tittl, *Adv. Mater.* **2022**, *35*, 2209688.

[34] A. L. Crook, C. P. Anderson, K. C. Miao, A. Bourassa, H. Lee, S. L. Bayliss, D. O. Bracher, X. Zhang, H. Abe, T. Ohshima, *Nano Lett.* **2020**, *20*, 3427.
[35] S. Sun, J. L. Zhang, K. A. Fischer, M. J. Burek, C. Dory, K. G. Lagoudakis, Y. K. Tzeng, M. Radulaski, Y. Kelaita, A. Safavi-Naeini, *Phys. Rev. Lett.* **2018**, *121*, 083601.
[36] J. D. Joannopoulos, P. R. Villeneuve, S. Fan, *Nature* **1997**, *386*, 143.
[37] D. Chugh, J. Wong-Leung, L. Li, M. Lysevych, H. H. Tan, C. Jagadish, *2D Mater.* **2018**, *5*, 045018.
[38] T. A. Chen, C. P. Chuu, C. C. Tseng, C. K. Wen, H.-S. P. Wong, S. Pan, R. Li, T. A. Chao, W. C. Chueh, Y. Zhang, *Nature* **2020**, *579*, 219.
[39] K. Watanabe, T. Taniguchi, H. Kanda, *Nat. Mater.* **2004**, *3*, 404.
[40] C. Fournier, A. Plaud, S. Roux, A. Pierret, M. Rosticher, K. Watanabe, T. Taniguchi, S. Buil, X. Quélin, J. Barjon, *Nat. Commun.* **2021**, *12*, 3779.
[41] X. Xu, Z. O. Martin, D. Sychev, A. S. Lagutchev, Y. P. Chen, T. Taniguchi, K. Watanabe, V. M. Shalaev, A. Boltasseva, *Nano Lett.* **2021**, *21*, 8182.
[42] L. Gan, D. Zhang, R. Zhang, Q. Zhang, H. Sun, Y. Li, C. Z. Ning, *ACS Nano* **2022**, *16*, 14254.
[43] J. C. Stewart, Y. Fan, J. S. H. Danial, A. Goetz, A. S. Prasad, O. J. Burton, J. A. Alexander-Webber, S. F. Lee, S. M. Skoff, V. Babenko, S. Hofmann, *ACS Nano.* **2021**, *15*, 13591.